

# Entanglement and geometric phase induced momentum quantization in a Stern-Gerlach interferometer

Atom Chip Group

*Department of Physics, Ben-Gurion University of the Negev, Be'er Sheva 84105, Israel*

## Abstract

Entanglement plays a central role in fundamental tests and practical applications of quantum mechanics. Meanwhile, topological physics has attracted great interest for the innovative conception of matter and the potential utilizations in quantum engineering, such as quantum metrology and quantum computing. Here we demonstrate a new tool for investigating entanglement and topology in the overlap of these two fields: an entanglement-induced momentum quantization, with an atom chip system. We entangle the internal (spin) and external (spatial) states of a two-level  $^{87}\text{Rb}$  atom via a sequence of radio-frequency pulses and pulsed magnetic field gradients from the atom chip, which evolves coherently along a non-cyclic geodesic path to form a stable spatial interference pattern. If we prepare the wave packets with maximum entanglement to enclose the origin of the Bloch sphere, the interference wavelength is quantized as the momentum kick from the atom chip changes, exhibiting the quantized Stern-Gerlach effect. In contrast, in the absence of the entanglement, the wavelength of the spatial interference is a continuous function of the imparted momentum kick. Finally, we discuss how this miniaturized device enables improvements in geometric quantum computing, quantum sensing, and the debate on the foundation of quantum mechanics.

**Introduction:** Entanglement is one of the most fundamental features of quantum mechanics. It is expected to be a primary resource for the expected speed-up in quantum computations or information. Single-particle entanglement (SPE), namely entanglement between different degrees of freedom of the same particle, is the subject of ongoing investigations [1–3]. The single-particle entanglement has been created via coupling the internal and external degree of freedom, for example, the Schrödinger cat experiment with a single ion [4]. SPE’s importance stems from its possible application as a resource in quantum information, quantum computation, or in the study of contextuality [5–8] in the foundation of quantum mechanics. More precisely, a neutron interference experiment [2] reported that SPE could check local hidden-variable theories with Bell-like inequalities emerging from local non-contextuality [3].

The Stern-Gerlach (SG) experiment is perhaps the earliest and simplest realization of

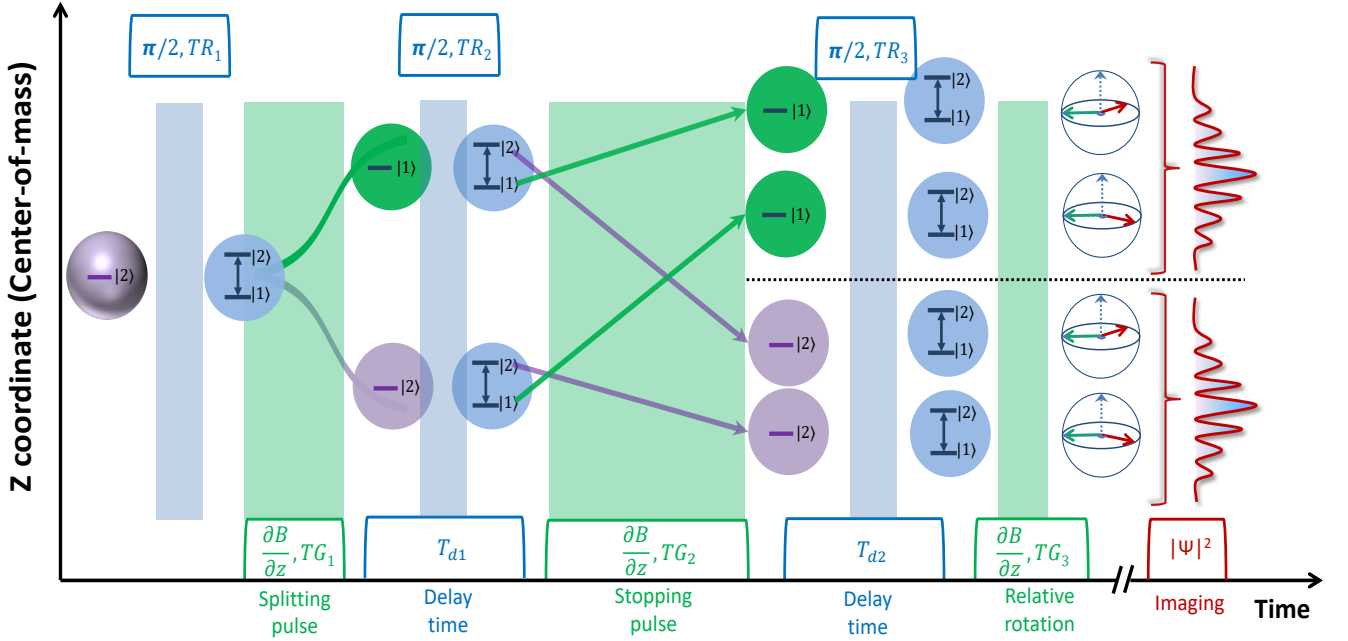


FIG. 1: **Experimental sequence of the quantized Stern-Gerlach experiment.** The evolution of the states along the sequence. After the atoms are released from the trap, one radio frequency  $\pi/2$  pulse ( $TR_1$ ) is applied to create a spin superposition for the Stern-Gerlach splitting, in which the different spins are exposed to a differential force created by a magnetic gradient pulse  $\partial B/\partial z$ , of duration  $TG_1$ , generated by currents in the atom chip wires. To stop the relative velocity of the wave packets and to close the interferometer loop, the second  $\pi/2$  pulse ( $TR_2$ ) is applied to mix the spins, and the second magnetic gradient pulse ( $TG_2$ ) is used to yield differential forces for the same-spin states with different locations. The system then consists of two wave packets with the relative-still momentum state (see text) in  $|2\rangle$  and two wave packets with the relative-still momentum state in  $|1\rangle$  (separated along the z-axis, the direction of gravity), and they are with different experimental zones. Afterward, the clock is initialized with a third RF pulse of duration  $TR_3$ , after which the relative rotation of the two clock wave packets may be changed by applying the third magnetic field gradient of duration  $TG_3$ . Last, before an image is taken, the wave packets can expand and overlap to form the interference pattern.

single-particle quantum entanglement [9–14]. In particular, SPE occurs in an SG interferometer through a beam splitter and magnetic gradient pulses. An atom chip with a miniaturized structure has offered a high level of spatial and temporal control of local fields,

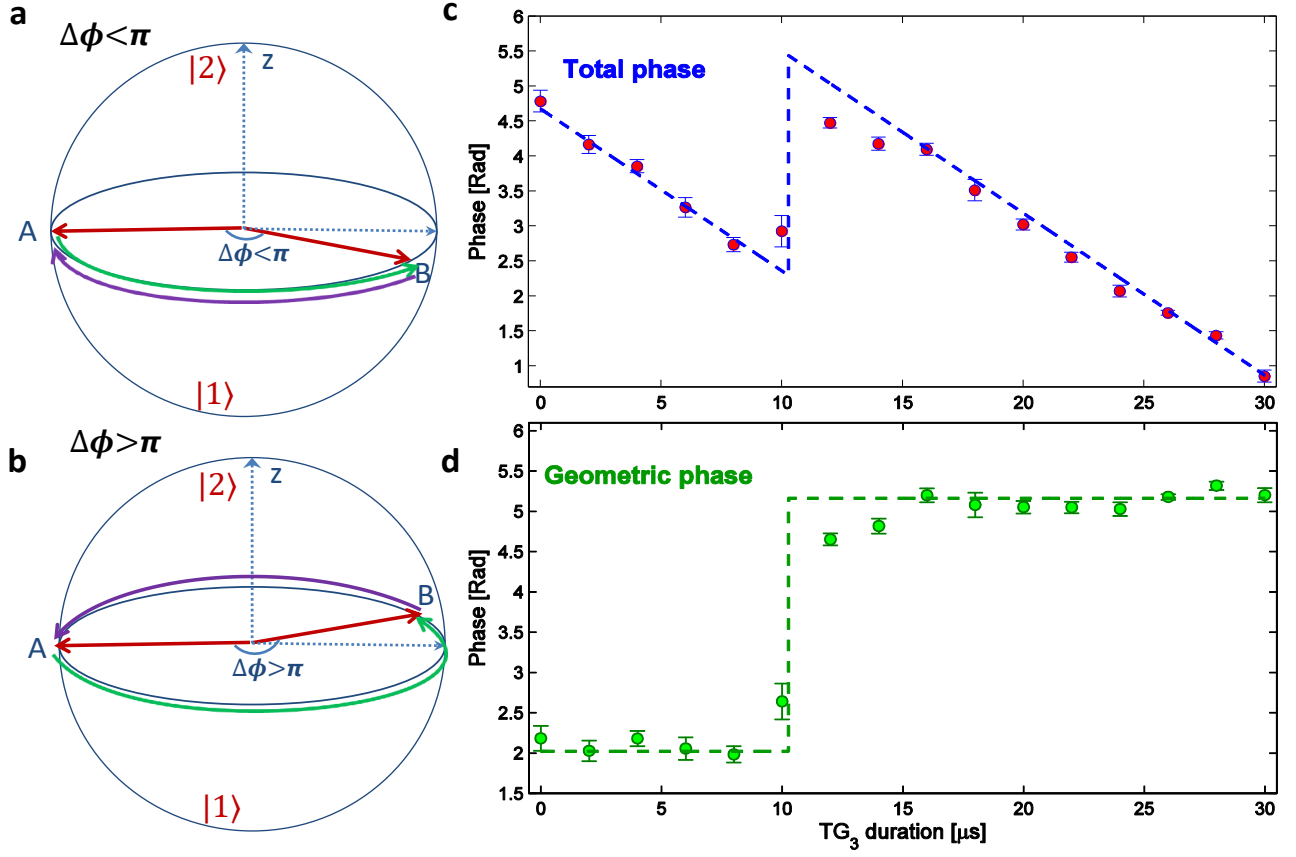


FIG. 2: **Quantized geometric phase.** (a) and (b), the geometric phase is decided by the enclosed area between the Hamiltonian line (red) and the geodesic connection (purple).

When  $\Delta\phi$  is smaller than  $\pi$ , the enclosed area is zero, corresponding to zero geometric phases no matter how large  $\Delta\phi$  changes within this range  $[0 \pi]$ . As long as  $\Delta\phi$  is larger than  $\pi$ , the enclosed area is the whole hemisphere, corresponding to  $\pi$  geometric phase no matter how large  $\Delta\phi$  changes within this range  $[\pi 3\pi]$ . (c), the measured total phase when

$TR_3 = \pi/2$ . Here the relative rotation between the two vectors is decided by

$\Delta\phi = \Delta E \times TG_3 / \hbar$ . As the two-level system consists of the  $mF=1$  and  $mF=2$  states, an

additional phase results from  $TG_3$ . The phase jump around  $TG_3 = 10 \mu s$  is obvious. (d),

the geometric phase with the strip of the dynamical phase. The phase rigidity and the  $\pi$  phase jump are clearly shown.

making it an ideal tool for creating entanglement through the SG experiment. We have recently shown that such an SG interferometer can generate a non-cyclic geometric phase [15]. The geometric phase [16] arising from non-cyclic transformations was first discussed theoret-

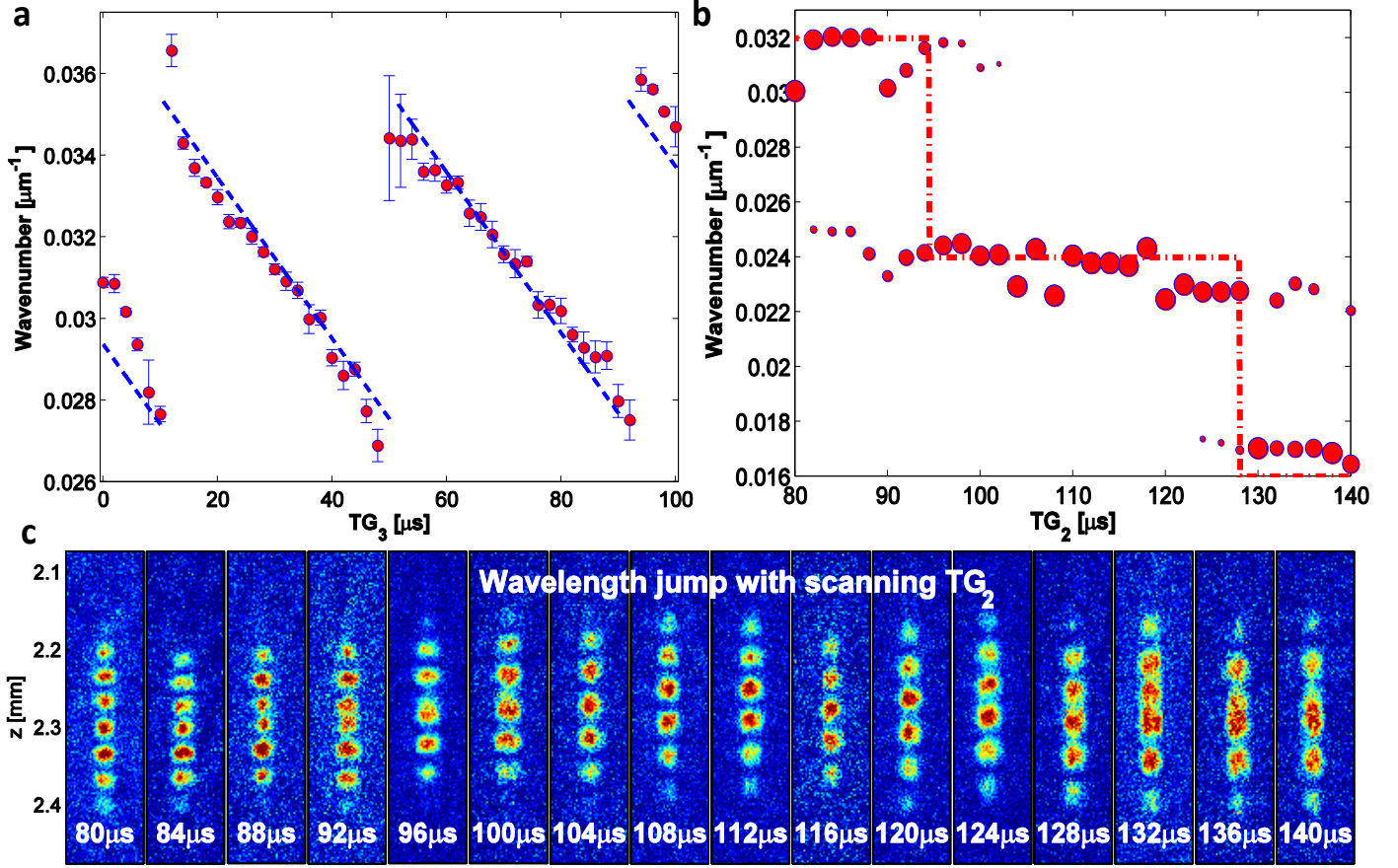


FIG. 3: **Quantized interferometric wavelength.** (a) Variation of the wavenumber as a function of  $TG_3$ , the entangler pulse. Since singular effects are seen only at or near maximum entanglement, the wavenumber displays a conventional linear dependence on  $TG_3$ , and the jumps are related to the change of ground state (see methods). (b), the summarized distribution of spatial frequency components. We observed the interferometric fringe periodicity constant with the varied magnetic fields,  $TG_2$ , which changes linearly (see Fig. 4). For specific magnetic fields, we observed abrupt downward spatial frequency jumps scaling as  $1/N$ , where  $N$  is an integer number 4, 3, and 2. the raw figures of the interferometric pattern when  $TG_2$  is scanned from  $80 \mu\text{s}$  to  $120 \mu\text{s}$ . (c), the raw CCD images corresponding to the wavenumber data presented in (b) (z-axis values are relative to the chip surface).

ically by Samuel and Bhandari [17]. The specific case of a two-level system was extensively explored in a subsequent work by Bhandari, who pointed out the occurrence of acute phase jumps during evolution [18, 19]. When the system evolves from point A to point B in

the Bloch sphere, the Pancharatnam phase is given minus half of the area enclosed by the trajectory AB and the shortest geodesic joining A and B. The phase jumps result from a sudden change of a geodesic when the system passes through specific points. These phase jumps have been observed experimentally in various methods, including, more recently, a matter-wave SG interferometer [15].

We study the synergy between the geometric phase and the SPE in an SG matter-wave experiment with Bose-Einstein Condensation (BEC) wave packets submitted to magnetic gradient pulses. These gradient pulses generate entanglement between the BEC atoms' spatial and spin degrees of freedom, affecting the interference wavelength. We find that when the wave-packets are not entangled, the wavelength of the spatial interference is a continuous function of the momentum kick imparted by the gradient pulses. But at maximum entanglement, it becomes quantized. This quantization arising in a continuous system is due to entanglement and the geodesic rule for the non-cyclic geometric phase.

**Experiment:** Our experimental scheme is depicted in Fig.1, consisting of radio-frequency Rabi transitions ( $TR$ s) between Zeeman sublevels and pulsed magnetic field gradients ( $TG$ s). In the SG effect, a magnetic field gradient exerts particles into different momenta according to their spin projections. The idea of exploiting this effect for creating coherent momentum superpositions for matter-wave interferometry has been demonstrated on an atom chip system [20–24]. The experiment starts by releasing  $^{87}\text{Rb}$  BEC atoms at  $|F, m_F\rangle = |2, 2\rangle$  from the magnetic trap, afterward, one radio-frequency  $\pi/2$  pulse ( $TR_1$ ) is applied to create a spin superposition ( $|F, m_F\rangle = |2, 1\rangle \equiv |1\rangle$ ) and  $|F, m_F\rangle = |2, 2\rangle \equiv |2\rangle$ ) for the SG splitting and recombining through  $TG_1$  and  $TG_2$ . The system then consists of two sets of wave-packets with the relative-still momentum state in  $|2\rangle$  and  $|1\rangle$  (separated along the z-axis, the direction of gravity), located in different experimental zones. Afterward, the spin superposition within each single-state wave-packet is initialized with a third RF pulse of duration  $TR_3$ , and the third magnetic field gradient of duration  $TG_3$  is applied. Last, the wave-packets experience time-of-flight expansion to form the interferometric pattern, and an absorption image is taken.

### Results:

In Fig. 2, we plot the total and geometric phases as functions of  $TG_3$ . The relative rotation between the two vectors on the equator of the Bloch sphere Fig.2(a-b) is expressed as  $\Delta\phi = \Delta E \times TG_3/\hbar$ . The results are shown in Fig.2(c-d). As stipulated by the geodesic

rule, there is a  $\pi$  phase jump in the total phase when the relative rotation between the two vectors  $\Delta\phi = \pi$ , and the geometric phase exhibits discrete plateaus.

After  $TG_2$ , we generate entanglement by applying the pulses  $TR_3$  and  $TG_3$ . Both pulses and the order of their application are crucial. If  $TR_3$  is applied without  $TG_3$ , this will rotate the spin of the wavepacket without inducing any entanglement. If  $TG_3$  is applied without  $TR_3$ , it will simply act as an extension of  $TG_2$  without affecting the factorization of spin and space. When both pulses are applied,  $TR_3$  has to come before  $TG_3$ . Reversing this order will be equivalent to applying  $TR_3$  after a longer  $TG_2$ , which does not yield entanglement. To reach maximum entanglement,  $TR_3$  and  $TG_3$  must be fine-tuned.  $TR_3$  must deliver equal populations in each spin state, i.e., we must be at the equator of the Bloch sphere (see methods).

The difference between  $TG_2$  and  $TG_3$  pulses in our sequence is illustrated in Fig. 3a-b when  $TR_3$  is set to a value with an equal population between  $|1\rangle$  and  $|2\rangle$ . When increasing  $TG_3$  (Fig. 3a), the wavenumber decreases linearly until  $TG_3$  reaches a value where it jumps and then decreases linearly again. This is because  $TG_3$  is the entangler pulse. At  $TG_3 = 0$ , the wavefunction is factorized between the spatial and the spin parts (see methods). A conventional linear dependence on  $TG_3$  is expected. When we increase  $TG_3$ , entanglement builds up until it reaches its maximum value. At maximum entanglement, the wavefunction cannot be written as a product of its spin and spatial part; this affects the interferometric wavenumber. We find that at the equator (equal population), the wavenumber is given by (see methods for details),

$$k_G = \frac{m\Delta z}{\hbar t} \frac{\cos \theta}{1 - \sin^2 \theta (1 - \cos \phi)}, \quad (1)$$

where the usual interference wavenumber  $k_0 = m\Delta z/\hbar t$  ( $m$  is the mass of the atoms,  $\Delta z$  the wavepacket separation, and  $t$  the time-of-flight) is modified by entanglement. We plot the wavenumber as a function of  $TG_2$  (Fig. 3b) when  $TG_3$  yields maximal entanglement. We observe plateaus followed by sharp jumps at specific values of  $TG_2$ . It should be noted that changing the splitting pulse  $TG_1$  instead of  $TG_2$  yields a similar behavior (see SM).

In Fig. 4, we analyze the role of the population of the spin states  $|1\rangle$  and  $|2\rangle$  on the wavelength quantization by varying  $TR_3$  when  $TG_3$  is set to the maximum entanglement point for equal population. To further prove that it is the entanglement that is responsible for the observed quantization of the interferometric wavenumber, we change entanglement

buildup by varying  $TR_3$  (Fig. 4(a-d)). When  $TR_3 = 0$ , the interferometer wavenumber changes linearly because the two wavefunctions are a product of spatial and spin parts and no area encloses the origin during evolution. However, we reach maximum entanglement (equal populations) in Fig. 4c, the Bloch sphere origin is enclosed, and we observe that the wavenumber is quantized. As shown in Eq. 1, in the presence of entanglement between the spatial and spin degrees of freedom, the wavenumber is renormalized by a term coming from the geometric phase (see methods), hence it displays singularities which were observed in the geometric phase [15]. This interpretation is supported by the excellent agreement between our model and experimental data (see methods for details).

**Outlook:** We report here the realization of a highly entangled spin-momentum single-particle state with sharp jumps of the geometric phase and interference wavelength in an SG interferometer. The occurrence of a robust geometric phase and the related wavelength rigidity, displayed by moving qubits, is a first step towards the extension of the holonomic quantum computing [25] to moving qubits.

Furthermore, the observed sharp jumps may also be used in a device for quantum sensing. A rotation sensing device can be built by adding three non-magnetic pulses in the transverse direction to our current configuration; the atoms can perform a half-loop enabling a Sagnac interferometer. Since we start with two wavepackets, this device is a dual gyroscope whose sensitivity can significantly be improved by setting the working point near the jump point and performing a differential analysis between the two double loops.

Finally, the single-particle entangled state observed here can play an essential role in the ongoing debate between quantum mechanics and hidden variables theories or other classical descriptions of physics[3]. Forty years after the Aspect experiment [26], non-locality in quantum mechanics is still not universally accepted [27–29]. At the single particle level, since the entanglement is local, the conflict between quantum mechanics and hidden variable theories is about contextual (quantum mechanics) [5, 6] and non-contextual (hidden variable) theories. The qualitative features displayed by entanglement in our experiment will shed new light on this debate.

## Methods

**Experimental method** We begin our experiment by preparing a BEC of about  $10^4$   $^{87}\text{Rb}$  atoms in the state  $|F, m_F\rangle = |2, 2\rangle$  in a magnetic trap located  $90 \pm 2$   $\mu\text{m}$  below the chip surface. The trap is created by a copper structure behind the chip with strong homogeneous



magnetic bias fields in the x, y, and z directions. After the BEC atoms are released from the trap, we start with applying  $TR_1$  (which is a radio-frequency (RF)  $\pi/2$  pulse of 10  $\mu$ s duration) to prepare the superposition of the  $|2\rangle \equiv |2, 1\rangle$  and  $|1\rangle \equiv |2, 1\rangle$  states. The entire sequence is done under a strong homogeneous magnetic bias field of 36.7 G in the  $y$  direction, which creates an effective two-level system via the non-linear Zeeman effect. This magnetic bias field is turned off before the imaging. Thus the absorption imaging is not sensitive to the Zeeman state, i.e., the atoms counting for  $|2\rangle$  and  $|1\rangle$  are weighed equally. After a 16-24 ms time-of-flight (where the different times correspond to different optimization depending on the parameter we scan), we image the atoms by absorption imaging and generate the picture shown in Fig. 3c.

All three magnetic gradient pulses are generated by three parallel gold wires on the chip surface, which are 10 mm long, 40  $\mu$ m wide, and 2  $\mu$ m thick. The wires' centers are separated by 100  $\mu$ m, and the same current runs through them in series, creating a 2D quadrupole field at  $z = 100$   $\mu$ m below the atom chip. The phase noise is mainly proportional to the magnitude of the magnetic field created during the gradient pulse. As the primary source of magnetic instability is in the gradient pulse originating from the chip, positioning the atoms near the middle (zero) of the quadrupole field created solely by the three chip wires 100  $\mu$ m below the chip surface reduces the phase noise during the operation. There is a 0.9ms waiting time between the trap release and the first gradient to let the atoms free fall from  $90 \pm 2$   $\mu$ m to approximately the quadrupole position of 100  $\mu$ m. The chip wire current was driven using a simple 12.5 V battery and was modulated using a homemade current shutter, with ON/OFF times as short as 1  $\mu$ s. The total resistance of the three chip wires is 13.6  $\Omega$ , yielding a current of  $11.3/13.6$  A  $\approx 0.83$  A (a small voltage drop exists in the circuit itself).

**Theory:** Here, we will show that the observed jumps in the interference wavenumber are due to the geodesic rule when space and spin variables are entangled. After the pulses,  $TR_3$  and  $TG_3$ , the wavefunctions are entangled between space and spin. They are given by:

$$|\psi_\alpha\rangle = \psi(z - z_1, t)e^{-ik_1z} \cos \frac{\theta}{2}|2\rangle + \psi(z - z_2, t)e^{-ik_2z} \sin \frac{\theta}{2}|1\rangle \quad (2)$$

$$|\psi_\beta\rangle = \psi(z - z_3, t)e^{-ik_3z} \cos \frac{\theta}{2}|2\rangle + \psi(z - z_4, t)e^{-ik_4z} \sin \frac{\theta}{2}|1\rangle. \quad (3)$$

where after some time of flight  $t$  the wavefunction is given by,

$$\psi(z - z_\ell, t) = \frac{\exp - \frac{(z - z_\ell - \hbar k_\ell t/m)^2}{4\sigma^2(1 + i\hbar t/2\sigma^2 m)}}{\sqrt{2\pi(1 + i\hbar t/2\sigma^2 m)}}. \quad (4)$$

Taking  $\langle \psi_\alpha | \psi_\beta \rangle$  we obtain an expression for the relative phase  $\Phi$  between the two states,

$$\tan \Phi = \frac{\cos^2 \frac{\theta}{2} \sin \phi_1(z) - \sin^2 \frac{\theta}{2} \sin \phi_2(z)}{\cos^2 \frac{\theta}{2} \cos \phi_1(z) + \sin^2 \frac{\theta}{2} \cos \phi_2(z)} \quad (5)$$

where

$$\phi_{1,2}(z) = \frac{\hbar t[(z - z_{1,2} - \hbar k_{1,2} t/m)^2 - (z - z_{3,4} - \hbar k_{3,4} t/m)^2]}{8\sigma^4 m(1 + \hbar^2 t^2/4\sigma^2 m^2)} + (k_{1,2} - k_{3,4})z. \quad (6)$$

It should be noted that if  $\phi_1(z) = 0$ , we retrieve the expression of the Pancharatnam phase [15, 18]. The Pancharatnam phase displays sharp jumps at the equator. This is the consequence of the geodesic rule for the non-cyclic geometric phase as discussed in Ref. [18]. The sharp phase jumps are due to the geodesic change in the spherical triangle that defines the Pancharatman phase. The interference wavenumber  $k_G$  is given by,  $k_G = d\Phi/dz$ . We find,

$$k_G = \frac{d\phi(z)}{dz} \frac{\cos \theta}{1 - \frac{1}{2} \sin \theta (1 - \cos \phi)} \quad (7)$$

where the prefactor  $d\phi/dz$  is the usual interference wavenumber in the presence of momentum corrections. It reads,

$$\frac{d\phi(z)}{dz} = \frac{\hbar t \Delta z + \hbar^2 t^2 \Delta k}{\hbar^2 t^2/m + 4\sigma^4 m}. \quad (8)$$

Hence Eq. 7 shows that the wavenumber  $k = \frac{d\phi(z)}{dz}$  at the pole is renormalized by the geometric phase in the presence of spin-momentum entanglement which occurs when the system is rotated out of a pole. When  $\Delta k$  is small and neglecting the term  $4\sigma^4 m$ , which is also small, we retrieve the usual expression  $k_0 = m\Delta z/\hbar t$ . In the following, we will neglect these terms,  $k_G$  reduces to,

$$k_G = \frac{m\Delta z}{\hbar t} \frac{\cos \theta}{1 - \sin^2 \theta (1 - \cos \phi)} \quad (9)$$

In Fig. S1, we display  $k_G/k_0$ . It is made of a series of peaks that become sharper as one moves from the poles toward the equator. At the equator, the pattern becomes a Dirac comb. This is a consequence of the geodesic rule for the Pancharatnam phase [18, 19]. To compare

this prediction with the experiment where each data point corresponds to an integration over hundreds of pixels, it is necessary to adopt a more suitable definition of  $\tilde{k}_G$ ,

$$\tilde{k}_G = \int_0^{TG_2} \frac{dk(TG_2)}{dT G_2} \frac{\cos \theta}{1 - \frac{1}{2} \sin^2 \theta (1 - \cos \phi(TG_2))} dTG_2, \quad (10)$$

Finally, we analyze the effect of entanglement on the wave number by taking the experimental value of  $\frac{dk(TG_2)}{dT G_2}$  at the north pole. For the values of the parameters used in the experiment,  $k(TG_2)$  is a linear function,  $k(TG_2) = -0.0003111TG_2 + 0.5923$ , and  $\phi(TG_2)$  is also linear,  $\phi(TG_2) = -0.1873TG_2 + 360.12$ . After plugging these expression in the integral in Eq. 10, we obtain the theoretical curves displayed in Fig. S2.

It should also be noted that if we rewrite the wavefunctions in Eq.3 into the spin-rotated basis  $|+\rangle = (|2\rangle + |1\rangle)/\sqrt{2}$  and  $|-\rangle = (|2\rangle - |1\rangle)/\sqrt{2}$ , neglecting the small difference in position between the  $|2\rangle$  and  $|1\rangle$  in the same wavefunction, i.e. assuming  $z_1 = z_2 = z_c$ , since  $k_1 = 2k_2$  we get for instance for  $|\psi_\alpha\rangle$  and  $\theta = \pi/2$ ,

$$|\psi_\alpha\rangle = \psi(z - z_c, t) e^{-ik_2 z} (\cos k_2 z |+\rangle + \sin k_2 z |-\rangle), \quad (11)$$

which means that  $TG_3$  modulates the populations between the states  $|+\rangle$  and  $|-\rangle$ .  $|\psi_\alpha\rangle$  is maximally entangled when there is an equal population between these states. This corresponds to  $k_2 z = (2n + 1)\frac{\pi}{4}$ .

- 
- [1] M. O. Terra Cunha, J. A. Dunningham, and V. Vedral, Entanglement in single-particle systems, *Proc. R. Soc. A* (2007) **463**, 2277.
  - [2] Y. Hasegawa, Entanglement Between Degrees of Freedom in a Single-Particle System Revealed in Neutron Interferometry, *Found. Phys.* (2012) **42**, 29.
  - [3] S. Azzini, S. Mazzucchi, V. Moretti, D. Pastorello, and L. Pavesi, Single-Particle Entanglement, *Adv. Quantum Technol.* **3**, 2000014, 2020.
  - [4] C. Monroe, D. M. Meekhof, B. E. King, and D. J. Wineland, A ‘‘Schrödinger Cat’’ Superposition State of an Atom, *Science*, 272, 1131-1136 (1996).
  - [5] A. Peres, Incompatible results of quantum measurements, *Phys. Lett. A* **151**, 107 (1990).
  - [6] N. D. Mermin, Hidden variables and the two theorems of John Bell, *Rev. of Mod. Phys.*, **65**, 803 (1993).

- [7] G. Jaeger, Quantum contextuality in the Copenhagen approach, *Phil. Trans. R. Soc. A* **377**: 20190025 (2019).
- [8] R. B. Griffiths, Quantum measurements and contextuality, *Phil. Trans. R. Soc. A* **377**: 20190033 (2019).
- [9] G. Reinisch, Stern–Gerlach experiment as the pioneer – and probably the simplest – quantum entanglement test? *Phys. Lett. A* **259**, 427 (1999).
- [10] G. B. Roston, M. Casas, A. Plastino, and A. R. Plastino, Quantum entanglement, spin-1/2 and the Stern–Gerlach experiment, *Eur. J. Phys.* **26** (2005) 657.
- [11] M. Singh, Quantum Stern-Gerlach experiment and path entanglement of a Bose-Einstein condensate, *Phys. Rev. A* **95**, 043620 (2017).
- [12] W. Gerlach and O. Stern, Der experimentelle Nachweis der Richtungsquantelung im Magnetfeld, *Z. Phys.* **9**, 349 (1922).
- [13] Editorial, The split of the century. *Nat. Phys.* **18**, 1381 (2022).
- [14] M. O. Scully, W. E. Lamb Jr., and A. Barut, On the theory of the Stern-Gerlach apparatus, *Found. Phys.* **17**, 575 (1987).
- [15] Z. Zhou, Y. Margalit, S. Moukouri, Y. Meir, and R. Folman, An experimental test of the geodesic rule proposition for the non-cyclic geometric phase, *Sci. Adv.* **6**, eaay8345 (2020).
- [16] M. Berry, Quantal phase factors accompanying adiabatic changes, *Proc. R. Soc. Lond. A* **392**, 45-57 (1984).
- [17] J. Samuel and R. Bhandari General Setting for Berry’s Phase, *Phys. Rev. Lett.* **60**, 2339 (1988).
- [18] R. Bhandari, "SU(2) phase jumps and geometric phases", *Phys. Lett. A* **157**, 221 (1991).
- [19] R. Bhandari, "The nonmodular topological phase and phase singularities," *Phys. Lett. A* **375**, 3562 (2011).
- [20] S. Machluf, Y. Japha, and R. Folman, Coherent Stern-Gerlach momentum splitting on an atom chip. *Nat. Commun.* **4**, 2424 (2013).
- [21] Y. Margalit, Z. Zhou, S. Machluf, D. Rohrlich, Y. Japha, and R. Folman, A self-interfering clock as a “which path” witness, *Science* **349**, 1205 (2015).
- [22] Z. Zhou, Y. Margalit, D. Rohrlich, Y. Japha, and R. Folman, Quantum complementarity of clocks in the context of general relativity, *Class. Quantum Grav.* **35**, 185003 (2018).
- [23] Y. Margalit, O. Dobkowski, Z. Zhou, O. Amit, Y. Japha, S. Moukouri, D. Rohrlich, A.

- Mazumdar, S. Bose, C. Henkel, and R. Folman, Realization of a complete Stern-Gerlach interferometer: Toward a test of quantum gravity, *Sci. Adv.* **7**, eabg2879 (2021).
- [24] O. Amit, et al. Anomalous periodicity in superpositions of localized periodic patterns. *New J. Phys.* **24** 073032 (2022).
- [25] E. Sjöqvist, D. M. Tong, L. M. Andersson, B. Hessmo<sup>1</sup>, M. Johansson, and K. Singh Non-adiabatic holonomic quantum computation, *New J. of Physics* **14** (2012) 103035.
- [26] A. Aspect, J. Dalibard, and G. Roger, Experimental Test of Bell's Inequalities Using Time-Varying Analyzers, *Phys. Rev. Lett.* **49**, 1804 (1982).
- [27] Accardi, L. (1984). The Probabilistic Roots of the Quantum Mechanical Paradoxes. In: Diner, S., Fargue, D., Lochak, G., Selleri, F. (eds) *The Wave-Particle Dualism. Fundamental Theories of Physics*, vol 3. Springer, Dordrecht.
- [28] M. O. Scully, N. Erez, E. S. Fry, Do EPR-Bell correlations require a non-local interpretation of quantum mechanics? I: Wigner approach, *Phys. Lett. A* **347**, 56 (2005).
- [29] A. Yu. Khrennikov, EPR–Bohm Experiment and Bell's Inequality: Quantum Physics Meets Probability Theory, *Theoretical and Mathematical Physics*, **157(1)**: 1448–1460 (2008).
- [30] T. M. Nieuwenhuizen, Is the Contextuality Loophole Fatal for the Derivation of Bell Inequalities?, *Found Phys* (2011) **41**: 580–591.

Supplementary material for

**Entanglement and geometric phase induced momentum  
quantization in a Stern-Gerlach interferometer**

Atom Chip Group

*Department of Physics, Ben-Gurion University of the Negev, Beer-Sheva 84105, Israel*

This file includes

Fig. [S1](#) Scaled interference wavenumber  $k_G/k_0$  as a function of the relative phase  $\phi(z)$  for different values of the colatitude  $\theta$ .

Fig. [S2](#) Integrated interference wavenumber  $\tilde{k}_G$  as a function of the pulse time  $TG_2$  for different values of the colatitude  $\theta$ .

Fig. [S3](#) The raw CCD images corresponding to the wavenumber data presented in Fig.4c, when  $TG_2$  is scanned from  $80\mu s$  to  $120\mu s$  while the maximized entanglement is prepared.

Fig. [S4](#) The raw CCD images, wavenumber and visibility data when  $TG_1$  is scanned from  $1.5\mu s$  to  $3.7\mu s$  while the maximized entanglement is prepared.

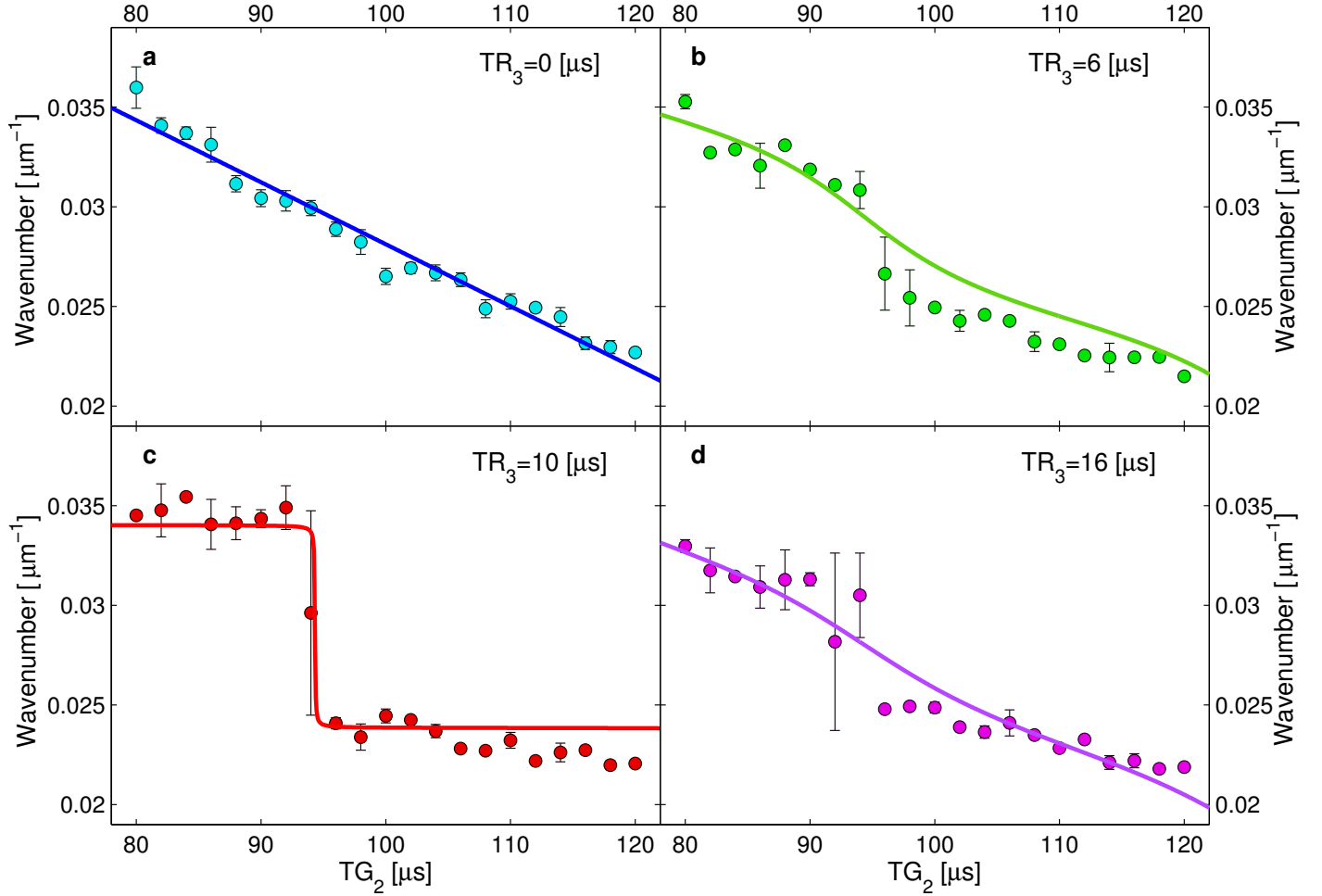


FIG. 4: **Varying the entanglement preparation.** To further prove that it is the entanglement preparation that is responsible for the observed quantization in wavenumber, we set  $TG_3$  to the maximum entanglement point, and we modulate the very formation of the superposition by varying  $TR_3$  so that the system preparation alternates between the maximized entanglement and no entanglement at all.  $TR_3$  with  $10\mu\text{s}$  corresponds to  $\pi/2$ . (a) When the value of  $TR_3$  is 0, it is just a single-state interference, and there is no GP accumulated. In this situation, the wavenumber changes linearly with  $TG_2$ . (b) When  $TR_3$  is larger than 0, and there is population transfer, the entanglement is formed, and the geometric phase accumulates. The linearity between the wavenumber and  $TG_2$  is influenced by the geometric phase and displays the renormalization by a term coming from the geometric phase. (c) When the imparted pulse duration of  $TR_3$  is  $10\mu\text{s}$ , the quantization happens. (d), When  $TR_3$  is larger than  $10\mu\text{s}$ , the system consists more  $|1\rangle$  population than  $|2\rangle$  but shows similar behaviors with (b). The error bars are the standard deviation of several data points.

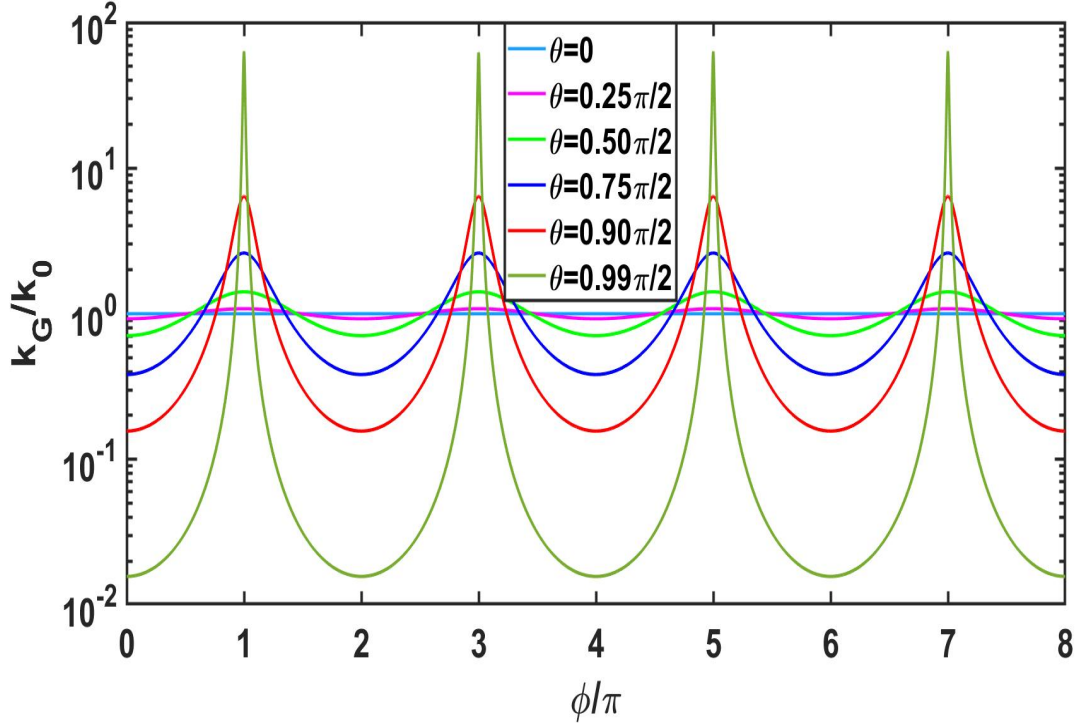


FIG. S1: Scaled interference wavenumber  $k_G/k_0$  as a function of the relative phase  $\phi(z)$  for different values of the colatitude  $\theta$ .  $k_G/k_0$  displays maxima at odd integer values of  $\phi$ . As  $\theta$  increases towards  $\pi/2$ ,  $k_G/k_0$  converges towards a Dirac comb. This is the consequence of the geodesic rule: when  $\theta = \pi/2$ , the Pancharatnam phase suddenly jumps when  $\phi$  crosses  $\pi$ . This is due to a sudden change of geodesic in the spherical triangle that defines the Pancharatnam phase on the Bloch sphere [18]. This corresponds to a 'momentum kick' for the wavenumber.



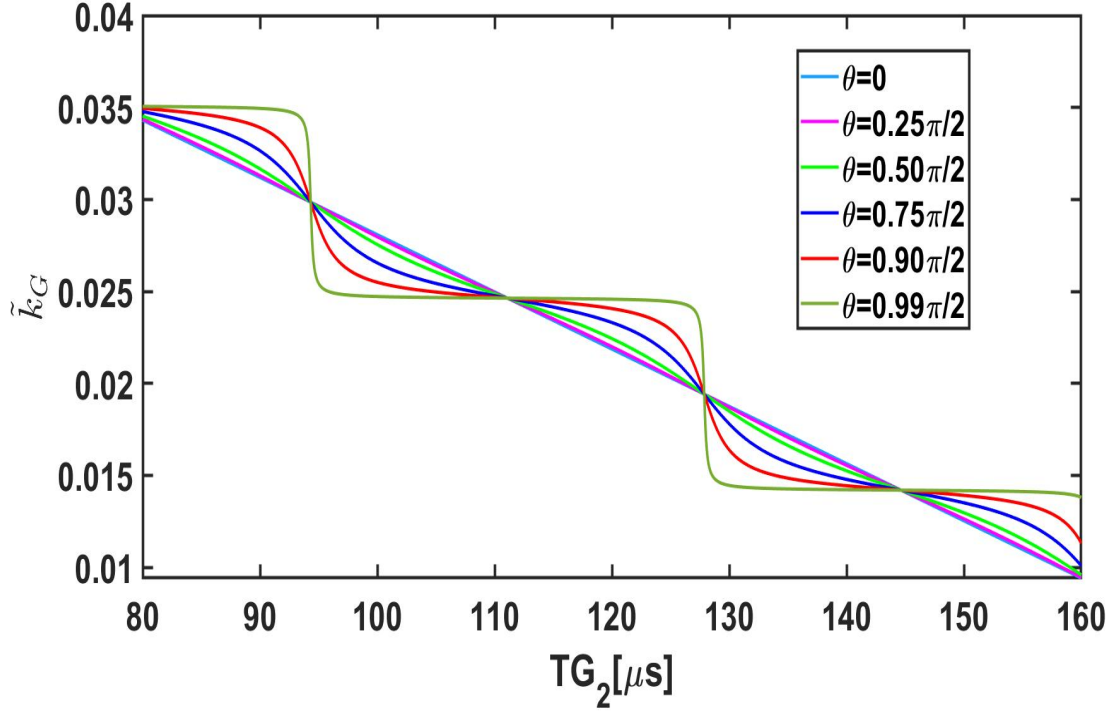


FIG. S2: Integrated interference wavenumber  $\tilde{k}_G$  as a function of the pulse time  $TG_2$  for different values of the collatitude  $\theta$ .  $\tilde{k}_G$  displays sharp jumps when  $\theta$  approaches  $\pi/2$ .

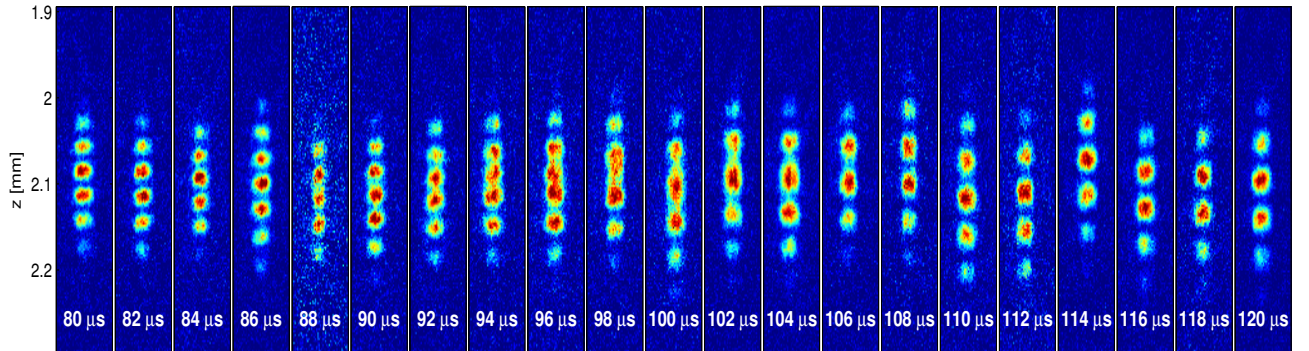


FIG. S3: The raw figures of the interferometric patterns in Fig.4c when  $TG_2$  is scanned from  $80 \mu s$  to  $120 \mu s$ . The entanglement is prepared with maximum.

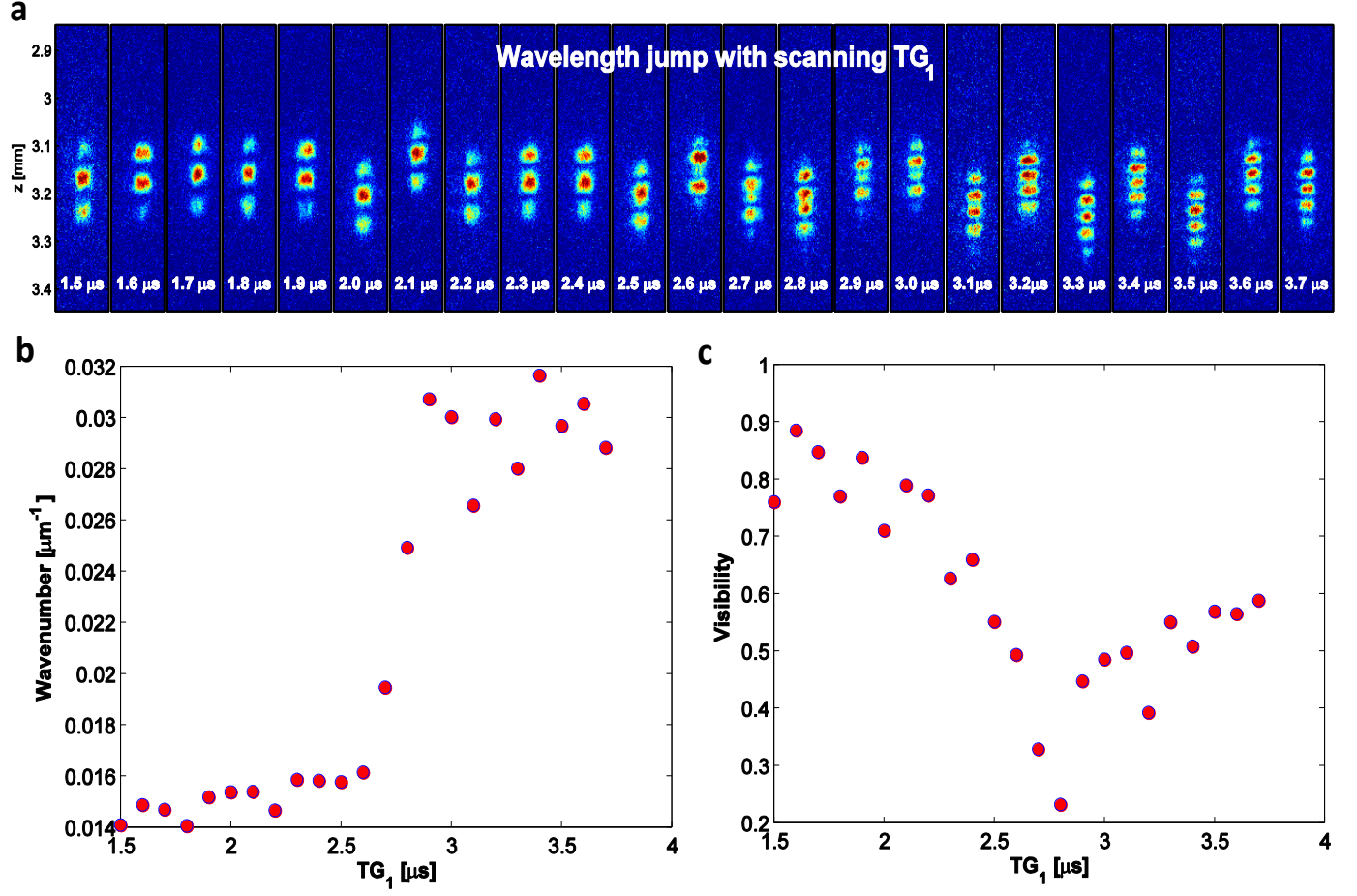


FIG. S4: **a:** The raw figures of the interferometric pattern when  $\text{TG}_1$  is scanned from 1.5  $\mu\text{s}$  to 3.7  $\mu\text{s}$ . **b,** The corresponding wavenumbers of the interferometric patterns when  $\text{TG}_1$  is scanned. **c,** The corresponding visibilities of the interferometric patterns when  $\text{TG}_1$  is scanned. The local minimum correspond to the place (2.7  $\mu\text{s}$ ) when the wavelength jump happens in **a** and **b**.